scientific reports

OPEN

Molsidomine provides neuroprotection against vincristine-induced peripheral neurotoxicity through soluble guanylyl cyclase activation

Irina Utkina-Sosunova[1,2,3,10], Alessia Chiorazzi[4,10], Mariangels de Planell-Saguer[1,2,3], Hai Li[5,6], Cristina Meregalli[4], Eleonora Pozzi[4], Valentina Alda Carozzi[4], Annalisa Canta[4], Laura Monza[4], Paola Alberti[4,7], Giulia Fumagalli[4], Charles Karan[5,6], Yalda Moayedi[3,8], Serge Przedborski[1,2,3,9], Guido Cavaletti[4,7] & Francesco Lotti[1,2,3✉]

Peripheral neurotoxicity is a dose-limiting adverse reaction of primary frontline chemotherapeutic agents, including vincristine. Neuropathy can be so disabling that patients drop out of potentially curative therapy, negatively impacting cancer prognosis. The hallmark of vincristine neurotoxicity is axonopathy, yet its underpinning mechanisms remain uncertain. We developed a comprehensive drug discovery platform to identify neuroprotective agents against vincristine-induced neurotoxicity. Among the hits identified, SIN-1—an active metabolite of molsidomine—prevents vincristine-induced axonopathy in both motor and sensory neurons without compromising vincristine anticancer efficacy. Mechanistically, we found that SIN-1's neuroprotective effect is mediated by activating soluble guanylyl cyclase. We modeled vincristine-induced peripheral neurotoxicity in rats to determine molsidomine therapeutic potential in vivo. Vincristine administration induced severe nerve damage and mechanical hypersensitivity that were attenuated by concomitant treatment with molsidomine. This study provides evidence of the neuroprotective properties of molsidomine and warrants further investigations of this drug as a therapy for vincristine-induced peripheral neurotoxicity.

Chemotherapy-induced peripheral neurotoxicity (CIPN) is a severe and dose-limiting adverse sequela of many antineoplastic drugs. These include platinum compounds, taxanes, vinca alkaloids, proteasome inhibitors, and other more targeted therapies such as ixabepilone and brentuximab vedotin, which are used against all of the most common types of cancer[1–5]. Cancer survival has increased significantly as oncological treatments have advanced, with many patients either being cured or living for many years with cancer. CIPN typically manifests as a length-dependent sensory axonal polyneuropathy with evidence of numbness/paresthesia and/or neuropathic pain in a stocking and glove distribution[1]. These symptoms contribute to functional comorbidities in day-to-day tasks due to the so-called sensory ataxia: the sensory loss can be so pronounced that fine manipulation and gate are impaired even in the absence of motor impairment[6,7]. The prevalence of CIPN varies from 20 to 80% during

[1]Center for Motor Neuron Biology and Disease, Columbia University, New York, NY 10032, USA. [2]Department of Pathology & Cell Biology, Columbia University, New York, NY 10032, USA. [3]Department of Neurology, Columbia University, New York, NY 10032, USA. [4]Experimental Neurology Unit, School of Medicine and Surgery, University of Milano-Bicocca, Monza, Italy. [5]Department of Systems Biology, Columbia University, New York, NY 10032, USA. [6]Sulzberger Columbia Genome Center, High Throughput Screening Facility, Columbia University Medical Center, New York, USA. [7]Fondazione IRCCS San Gerardo Dei Tintori, Monza, Italy. [8]Department of Otolaryngology-Head & Neck Surgery, Columbia University, New York, NY, USA. [9]Department of Neuroscience, Columbia University Medical Center, New York, USA. [10]These authors contributed equally: Irina Utkina-Sosunova and Alessia Chiorazzi. ✉email: fl2219@cumc.columbia.edu

treatment and depends on the chemotherapy regimen; however, neuropathy is at the highest level in the first month after completion of chemotherapy[8]. CIPN may present during chemotherapy, as is commonly seen with platinum-based and anti-tubulin compounds[9]. It may also occur after treatment—a phenomenon known as "coasting"—where either mild neuropathy worsens or new CIPN develops[10]. In as many as 30% of patients, pain and sensory abnormalities can persist for months or years after the cessation of chemotherapy[8]. As preventative or treatment options for CIPN are currently limited[11], dose reduction or cessation of chemotherapy is the only option after the emergence of symptoms that negatively impact patients' quality of life, duration, and efficacy of cancer treatment[12].

Vincristine (VCR) is the most widely used vinca alkaloid and effective anticancer agent for treating leukemia, lymphoma, and brain tumors in adults and children[13]. In addition to sensory neuropathy, VCR causes motor deficits that are observed as early as one week after commencing treatment[14,15]. Several drugs that may prevent pain, including glutamic acid, B-group vitamins, and amitriptyline, have been evaluated for preventing VCR-induced peripheral neurotoxicity (VIPN) in randomized, double-blind, placebo-controlled trials[16–18]. Unfortunately, no drugs have shown definite effects in patients treated with VCR suffering from VIPN. The failures of multiple clinical trials underscore the need to explore and address underlying mechanisms more broadly[19]. For example, for other chemotherapeutic agents, how VCR exposure induces neuropathy is not entirely understood. However, altered microtubules and mitochondrial dynamics, axon degeneration, and neuroinflammation are hallmarks of VIPN that when prevented, significantly impact symptoms manifestation[20–27].

One of the most striking discoveries regarding axon biology is the demonstration that the gain-of-function mutation, slow Wallerian degeneration (WldS), delays axon degeneration after nerve injury[28]. This Wallerian degeneration (WD) requires the pro-degenerative molecules sterile alpha and TIR motif-containing protein-1 (SARM1) and conversely, the nicotinamide mononucleotide adenylyltransferase-2 (NMNAT2) that is essential for axon growth and survival[29]. Interestingly, several signaling molecules on the SARM1 and NMNAT pathways that protect axons from WD can also impact CIPN[21,30–32]. Altogether, these findings suggest that axon degeneration is central to CIPN pathology, and strategies to prevent this process have significant therapeutic potential.

Here, we describe a comprehensive drug discovery platform to identify neuroprotective agents to halt VIPN. Among the hits identified, SIN-1—a nitric oxide (NO) donor—prevented VCR-induced axon loss in both motor and sensory neurons without compromising vincristine anticancer potency. We found that soluble guanylyl cyclase (sGC) inhibitors attenuated SIN-1 neuroprotection, while sGC activators mimicked SIN-1 effects, indicating that SIN-1 neuroprotection is functioning through sGC activation. To test SIN-1 therapeutic potential, we used an in vivo model of VIPN. VCR administration in rats induced severe sensory and motor neuropathy attenuated by concomitant treatment of rats with molsidomine—a SIN-1 pro-drug. Therefore, this study provides evidence of the neuroprotective properties of molsidomine in vivo and opens the way to further investigations of this drug as a therapeutic agent to prevent VIPN.

Results

High-throughput screening for small molecules that prevent vincristine-induced neurotoxicity

We developed a high-throughput neuron-based assay with genetically labeled mouse Embryonic Stem (ES) cell-derived motor neurons (ES-MNs) to identify modulators of VCR-induced axon degeneration. ES-MNs were differentiated[33–35], and dissociated cells were plated in 384-well plates. We developed an automated approach for fast quantitation of soma and neurite morphometry using a high-content imaging system to detect GFP-positive neurites and cell bodies, which gives robust measurements of neurite outgrowth in individual neurons (Suppl. Figure 1A). Since axon degeneration is a common process in CIPN, we posit that a relevant model of the disease should be able to monitor neurite degeneration rather than extension of existing neurites or outgrowth of new neurites. For this reason, we followed the survival and neurite outgrowth of ES-MNs for nine consecutive days and selected a time-point (five days in vitro [5 DIV]) when neurons no longer die or extend neurites (Suppl. Figure 1B–C). Of note, at this time-point, ES-MNs in culture fire action potentials and express pre- and post-synaptic markers, suggesting they are part of a functional neuronal network[34]. Using this setup, we tested the effect of increasing concentrations of VCR (10 pM–10 nM) on survival and neurite length of ES-MNs, aiming for the lowest VCR concentration that would induce robust damage without overt cell death. After 24 h, VCR induced a concentration-dependent reduction in neurite length, which up to 10 nM did not affect survival (Fig. 1A). To determine the optimal duration of exposure, we treated ES-MNs with 2 nM of VCR for an interval of 2 to 48 h and selected 24 h as the optimal exposure time (Fig. 1B). Treatment of ES-MNs with 2 nM of VCR for 24 h induced a robust and reproducible reduction in neurite length (≥75%) without affecting survival (Fig. 1A–C). We selected 2 nM of VCR for 24 h to model VCR-induced toxicity in vitro based on these results. To minimize well-to-well and plate-to-plate variations in the study, positional effects (e.g., edge effect) were excluded, the plate coating protocol was optimized, and medium evaporation was mitigated. With these adjustments, we reduced the mean coefficient of variation (CV) to $9 \pm 2\%$.

To validate the ability of our neuron-based assay to identify compounds that protect axons from VCR-induced toxicity, we screened a collection of biologically active molecules (Tocriscreen Plus). This library of 1,280 bioactive small molecules was selected for its wide range of pharmacological targets and research areas[36–38]. The primary screen was conducted at 10 µM in triplicate plates to minimize the occurrence of false negatives and positives. Compound toxicity was defined as a reduction of neuronal survival greater than 35% of DMSO control and was assessed by cell number quantitated by MetaMorph analysis and by ATP cellular content using a Celltiter Glo assay[39]. Toxicity results yielded 38 toxic compounds at 10 µM. In addition, 16 compounds showed high auto-fluorescence and were not analyzed further. To monitor axon degeneration, results from each well were expressed as a ratio of the neurite length per cell at T1 (24 h after treatment) over T0 (before treatment) and normalized to the mean of VCR-free control (DMSO) and expressed in percent. A snapshot of the data
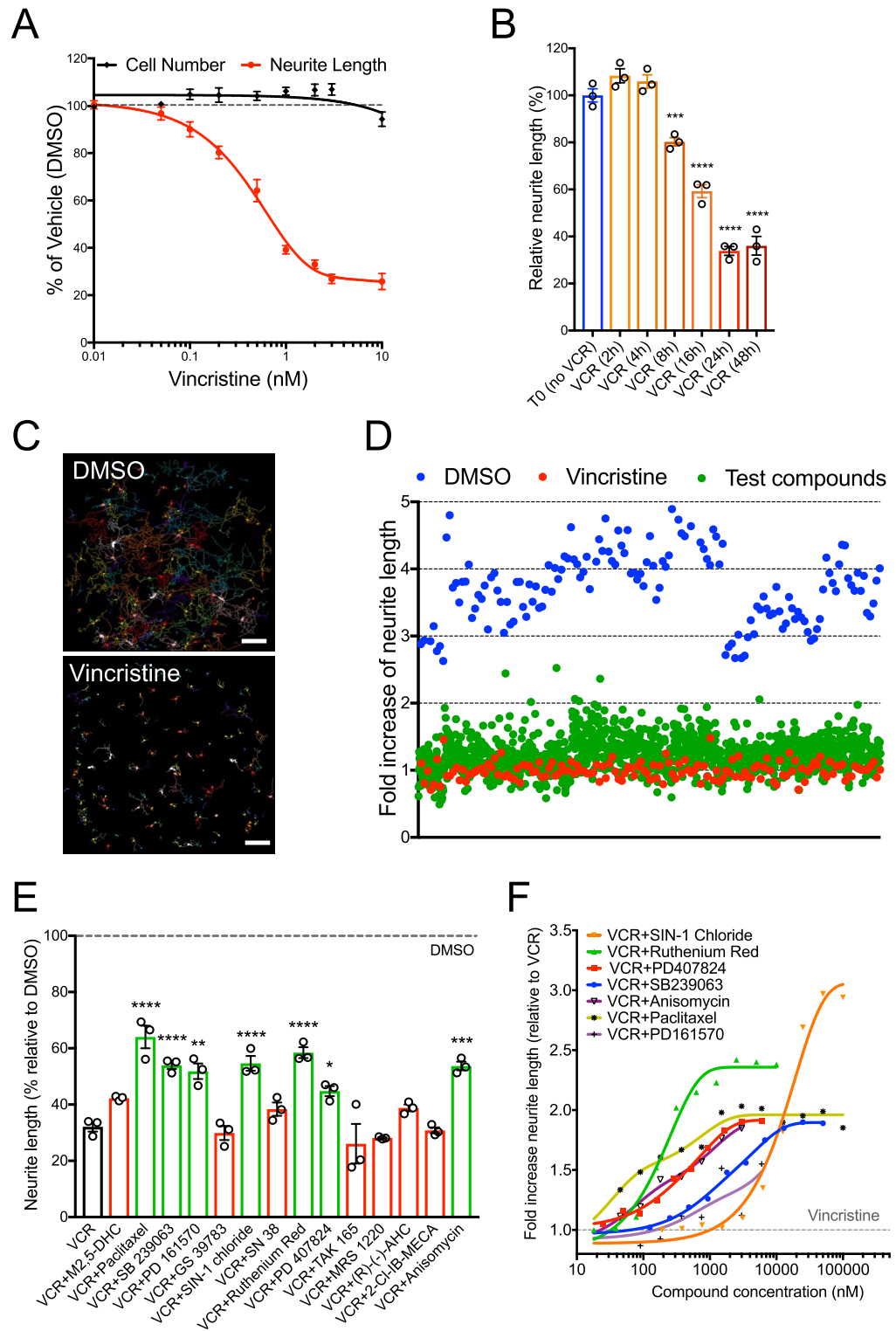
Figure 1. High-throughput screening for small molecules that prevent vincristine-induced neurotoxicity. (**A**) Dose-dependent effect of VCR on ES-MNs neurite length (red curve) and cell number (black curve). VCR doses are expressed in a log scale. Data are presented as Mean ± SEM of 3 independent experiments. (**B**) Time-dependent effect of 2 nM VCR on neurite length. Data are presented as Mean ± SEM of 3 independent experiments. One-way ANOVA, repeated measurements, with Dunnett's multiple comparison test (***$p = 0.001$; ****$p < 0.0001$ *vs.* no VCR). (**C**) Whole well images of alive GFP + ES-MN in 384 well plates were processed with MetaMorph for cell numbers and neurite length measurements and presented in pseudo colors. Scale Bars 250 µm (**D**) Snapshot of the screening data. Neurite outgrowth data are converted to fold-increase by normalizing them to VCR in each plate (red dots). Data collected from all 384-well plates are plotted for DMSO (blue dots) and test compounds (green dots). (**E**) Effect of 14 re-purchased candidates on neurite length. Results are presented in percent relative to DMSO (dotted line). Data are presented as Mean ± SEM of 3 independent experiments. One-way ANOVA, repeated measurements with Dunnett's multiple comparison test (*$p \leq 0.05$, **$p \leq 0.001$, ****$p \leq 0.0001$ *vs.* VCR). (**F**) Dose–response curves for 7 hits in the presence of 2 nM VCR treatment for 24 h. Traces are plotted as non-linear fit with a log scale in fold increase relative to VCR treated neurons (gray dashed line). All data are presented as Mean ± SEM of 3 independent experiments; error bars are not shown for clarity. See also Figure S1.

converted to fold-increase is reported in Fig. 1D. Of the 1,226 remaining bioactive small molecules, 14 met our hit criteria (i.e., ≥ 2.0 SD above the mean neurite length of all compound treated wells), which corresponded to a hit rate of 1.09%. Of these 14 initial hits, 7 retested positive in the same assay (Fig. 1E) and were further tested at ten increasing concentrations. All 7 compounds exhibited a concentration-dependent decrease in VCR-induced axon degeneration (Fig. 1F).

To further assess the effectiveness of our assay for high-throughput screening (HTS), we have followed the value of the Z factor[40]. While this factor does not rely on a distributional assumption, it best reflects the assay quality under normal distribution[41]. We calculated the Z factor of all plates in our screen (a total of 15 plates run over 5 weeks) and obtained an average Z factor of 0.62 ± 0.12, deemed excellent for a cell-based assay[41]. Thus, we established a consistent and robust cell-based phenotypic assay that accurately measures VCR-induced effects on neurite length of ES-MNs that is amenable to high-throughput chemical and genetic screens.

SIN-1 protects sensory and motor neurons from vincristine-induced neurotoxicity without interfering with vincristine anticancer activity

While high-throughput screens test many compounds over a short time, secondary assays aim to characterize further the activity and relevance of the most potent hits. Thus, we assessed our 7 lead compounds, first, in primary MNs (pMNs) from spinal cords of embryonic Hb9::GFP transgenic mice, which were dissected, dissociated to single cells[42,43], and plated in 96-well plates at 1,500 GFP + cells/well (Suppl. Figure 2A–C). pMNs were cultured for two days before addition of VCR (10 pM–100 nM). VCR effect on survival and neurite length of pMNs was determined 24 h after treatment. From this dose–response profile, we found that 1 nM VCR treatment induces a robust neurite retraction (> 70%) with minimal effect on cell survival; therefore, we selected this concentration of VCR for our cell-based assay with pMNs (Suppl. Figure 2D). Treatment with 1 nM of VCR for 24 h induced ~ 70% neurite degeneration in pMNs that was partially prevented by concomitant treatment with either SIN-1 (25 μM), ruthenium red (0.5 μM), PD407824 (3 μM), SB239063 (12.5 μM), or anisomycin (1.75 μM), while paclitaxel (1.75 μM) and PD161570 (1.75 μM) only marginally mitigated VCR-induced axonopathy (Fig. 2 A–B).

Aside from motor deficits, VCR can cause pain, paresthesia, numbness, and impaired touch. Thus, we also tested our 7 lead compounds for their activity in primary cultures of sensory neurons, using genetically labeled dorsal root ganglion (DRG) neurons as a source of sensory neurons. We dissected DRG neurons from 12-week-old *Pirt*::tdTomato transgenic mice. These mice express a red fluorescent protein (td-Tomato) in most DRG neurons (Suppl. Figure 2E–G)[44,45]. Sensory neurons were plated in 384-well plates and cultured for 5 days before adding VCR (10 pM–100 nM). VCR effect on survival and neurite length of DRG neurons was analyzed 24 h after its addition. We found that 4 nM VCR treatment induced a robust neurite degeneration without affecting cell survival; this concentration was used for subsequent cell-based assays with sensory neurons (Suppl. Figure 2H). Treatment with 4 nM of VCR for 24 h induced ~ 50% neurite degeneration in DRG neurons that was robustly prevented by concomitant treatment with 25 μM SIN-1, while the other primary hits did not prevent VCR-induced axonopathy (Fig. 2C–D). We subsequently focused on the most potent lead, SIN-1 (linsidomine), and its pro-drug molsidomine.

To translate these findings into a clinically relevant application, we examined whether the anticancer efficacy of VCR is affected by SIN-1 treatment. Accordingly, we developed a counter-screen using immortalized lines of lymphocytes derived from patients with T-cell acute lymphoblastic lymphoma (T-ALL) or B-cell Non-Hodgkin lymphoma (B-NHL; diffuse large cell), types of cancers commonly treated with VCR[46,47]. VCR-induced death was determined using a luminescent viability assay based on the quantitation of ATP (CellTiter-Glo®). Two cancer lines were treated either with VCR alone or with VCR and SIN-1. Treatment with VCR (0.01 nM–0.1 μM) showed a dose-dependent inhibition of cell survival (Fig. 2E–F, black curves). Compounds interfering with VCR apoptotic activity would shift the EC_{50} curve to the right, indicating reduced VCR efficacy in killing cancer cells. Results showed that 24-h co-treatment with SIN-1 (25 μM, the same dose that protects against VCR neurotoxicity) did not interfere with VCR anticancer activity (Fig. 2E–F, red curves).

Soluble guanylyl cyclase activation provides neuroprotection against vincristine-induced neurotoxicity

SIN-1 is the active metabolite of molsidomine (MOL), a nitric oxide (NO) mimetic used clinically for over 25 years[48]. MOL undergoes sequential degradation, initially via enzymatic conversion in the liver to SIN-1, followed by rapid decomposition at physiological pH to SIN-1A. SIN-1A is stable in anaerobic environments[49]. However, under biological conditions, oxidation of SIN-1A results in the production of molecular NO.

To investigate whether the NO donor activity of SIN-1 is required for its neuroprotection, we took advantage of the known decomposition of MOL in metabolites that can release NO (i.e., SIN-1 and SIN-1A) or do not release NO (i.e., SIN-1C)[49]. We tested these metabolites for their capacity to prevent VCR neurotoxicity in ES-MNs at differing dosages (Suppl. Figure 3). As expected, MOL did not show any neuroprotection as it needs to be enzymatically activated in the liver to give rise to its active metabolite SIN-1. Interestingly, while SIN-1 and SIN-1A showed neuroprotection, SIN-1C did not, suggesting that NO release is essential to mitigate VCR neurotoxicity (Suppl. Figure 3).

One of the most established functions of SIN-1 is to activate soluble guanylyl cyclase (sGC) and increase the levels of guanosine 3',5'-cyclic monophosphate (cGMP)[50]. Therefore, we used cGMP levels as a proxy of sGC activity to assess whether SIN-1 can activate this enzyme in our in vitro model of motor and sensory neurons. Remarkably, a 4-h treatment of ES-MNs with SIN-1 resulted in a ~ threefold increase in cGMP levels relative to the control in both neuronal types (Fig. 3A–B). SIN-1 effect on cGMP levels is dampened by ODQ, an irreversible inactivator of sGC[51] (Fig. 3A–B). In addition, VCR treatment reduced the levels of cGMP, suggesting that it
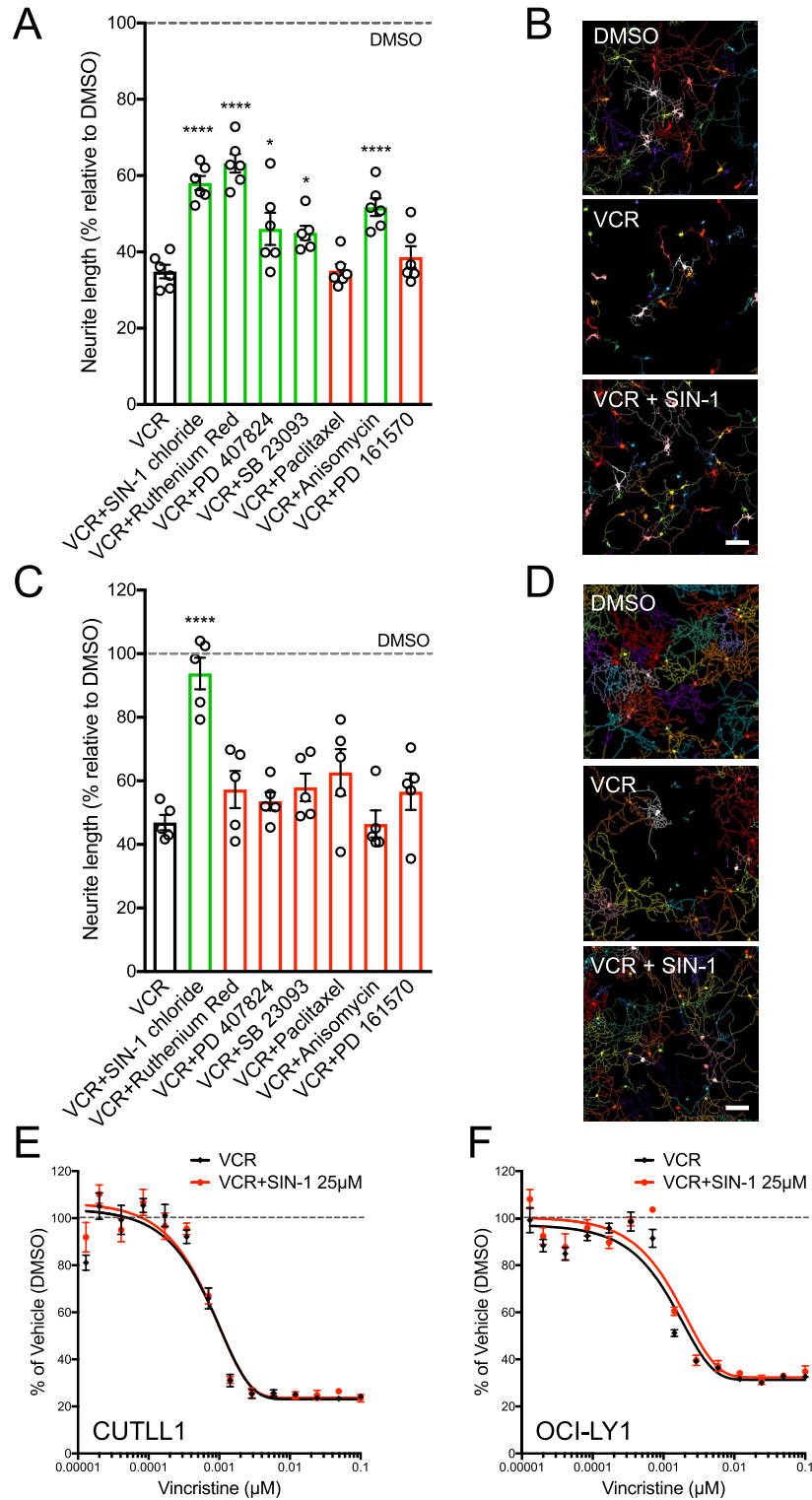
Figure 2. SIN-1 protects sensory and motor neurons from vincristine-induced neurotoxicity without interfering with vincristine anticancer activity. (**A**) Effect of 7 lead compounds on pMNs. Neurite length is expressed in percent relative to DMSO (dotted line). Data are presented as Mean ± SEM of 3 independent experiments. One-way ANOVA, repeated measurements with Dunnett's multiple comparison test (*$p \leq 0.05$, ****$p \leq 0.0001$ *vs.* VCR). (**B**) Representative MetaMorph converted images of GFP positive pMNs in control (0.1% DMSO), 1 nM vincristine (VCR), and 25 μM SIN-1 in the presence of 1 nM VCR (VCR + SIN-1). Scale bar, 100 μM. (**C**) Effect of 7 lead compounds on DRG neurons. Neurite length is expressed in percent relative to DMSO (dotted line). Data are presented as Mean ± SEM of 3 independent experiments. One-way ANOVA, repeated measurements with Dunnett's multiple comparison test (*$p \leq 0.05$, ****$p \leq 0.0001$ *vs.* VCR). (**D**) Representative MetaMorph converted images of td-Tomato positive DRG neurons in control (0.1% DMSO), 4 nM vincristine (VCR), and 25 μM SIN-1 in the presence of 4 nM VCR (VCR + SIN-1). Scale bar, 200 μm. (**E–F**) SIN-1 does not interfere with VCR anticancer activity in cancer lines: CUTLL1 (E) and OCI-LY1 (F). Luminescent cell viability assay based on ATP quantitation in proliferative cells treated with vincristine (VCR, black curves) and vincristine plus SIN-1 (VCR + SIN-1, red curves). VCR doses are expressed in a log scale. Data are presented as Mean ± SEM of 3 independent experiments. See also Figure S2.
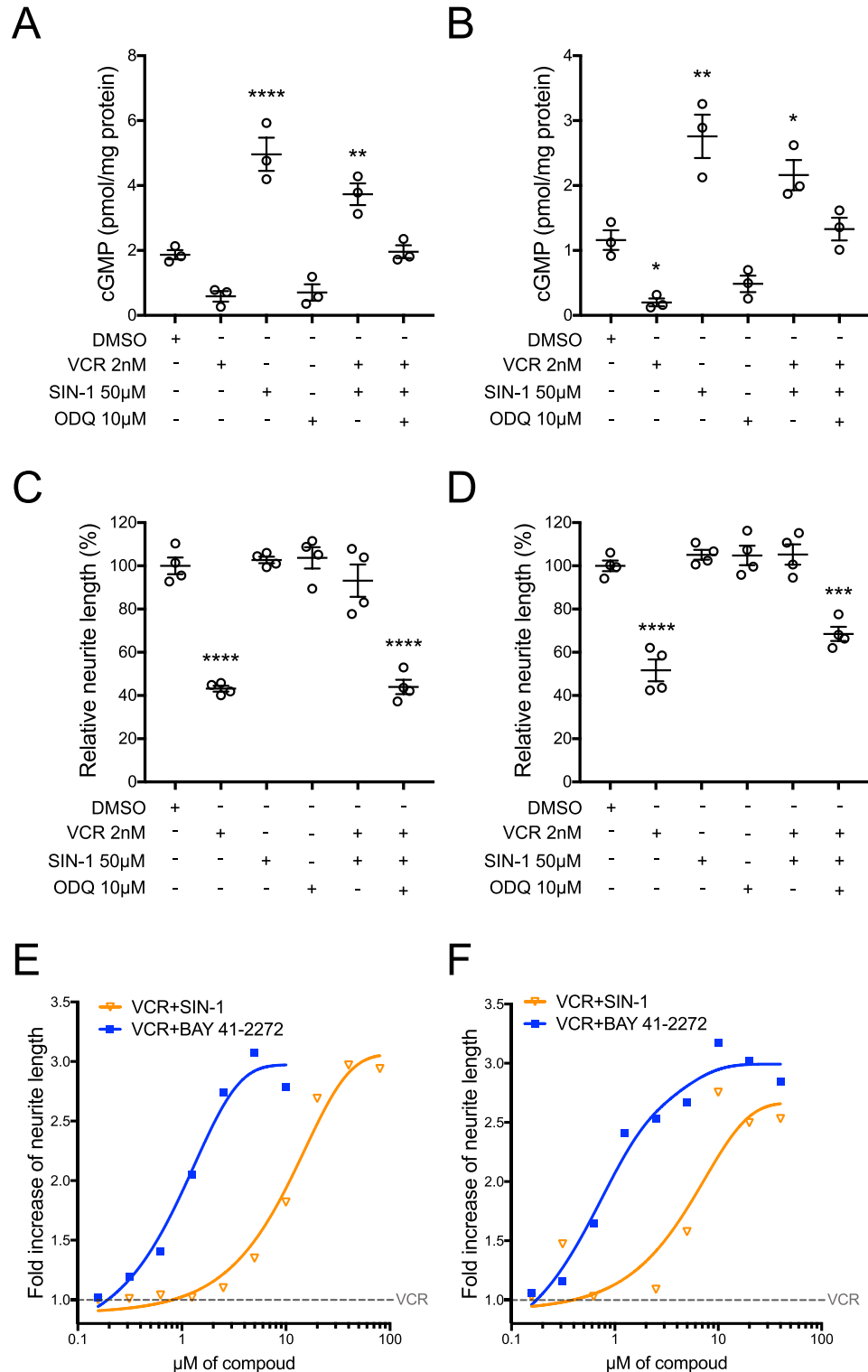
Figure 3. Soluble Guanylyl Cyclase activation provides neuroprotection against vincristine-induced neurotoxicity. (**A** and **B**) Levels of cGMP in ES-MNs (A) and DRG neurons (B) shown as a proxy of sGC activation. Data are presented as mean ± SEM of 3 independent experiments (one-way ANOVA for A: **$p = 0.0077$, ****$p < 0.0001$ relative to DMSO treated cells. One-way ANOVA for B: DMSO *vs* VCR *$p = 0.0468$, DMSO *vs* SIN-1 **$p = 0.0011$, DMSO *vs* VCR + SIN-1 *$p = 0.0363$,). (**C** and **D**) Effect of ODQ treatment on SIN-1 neuroprotective activity in ES-MNs (**C**) and DRG neurons (**D**). Values are means ± SEM of 4 biological replicates (one-way ANOVA: ***$p = 0.0002$, ****$p < 0.0001$ relative to DMSO treated cells). (**E** and **F**) sGC activators SIN-1 and BAY 41–2272 protect neurite length against VCR in ES-MNs (**E**) and DRG neurons (**F**). Doses of compounds are expressed in a log scale. Values are means of six technical replicates; error bars are not shown for clarity. See also Figure S3.

can act as an inhibitor of sGC (Fig. 3A–B). Importantly, this inhibiting effect of VCR on sGC is counteracted by concomitant treatment with SIN-1 in both motor and sensory neurons (Fig. 3A–B).

If the activation of sGC is required to mitigate VCR neurotoxicity, we hypothesized that inhibitors of sGC should dampen the neuroprotective activity of SIN-1. At the same time, sGC activators should be able to mimic SIN-1's effect. To test this hypothesis, we irreversibly blocked sGC with ODQ and found that SIN-1 can no longer protect ES-MNs and DRG neurons from VCR neurotoxicity (Fig. 3C–D). Then, we treated ES-MNs and DRG neurons with VCR in the presence of increasing concentrations of a well-established sGC activator (BAY 41-2272) and found that it can overcome VCR neurotoxicity at lower doses than SIN-1 (Fig. 3E–F). Altogether, these data suggest that sGC activation and cGMP levels are essential modulators of VCR-induced neurotoxicity.

Molsidomine provides neuroprotection in a rat model of vincristine-induced peripheral neurotoxicity

To explore the role of the SIN-1 neuroprotective effect in mature neurons in vivo, we used an extensively validated rat model of VIPN[52]. As mentioned above, SIN-1 is the active metabolite of MOL (Corvaton®), a drug used for many years to treat conditions such as ischemic heart disease, angina, and pulmonary hypertension[53]. Chronic administration of MOL in rodents is well tolerated, consistent with its clinical safety profile[54–57]. Therefore, MOL was used for our in vivo experiments.

In dose–response curves in vitro, SIN-1 is only effective at relatively high concentrations with an EC_{50} of 12.5 μM. Therefore, we sought to determine the level of SIN-1 accumulation in the plasma in rats treated with 20 mg/kg of MOL, a dose selected based on previous pharmacokinetics studies[57]. To do so, we orally administered MOL to 5 adult female rats and collected blood at time intervals between 5' and 24 h. Using liquid chromatography with tandem mass spectrometry, we found that the concentration of MOL-derived SIN-1 peaks around 7 μM in the plasma of rats treated with 20 mg/kg of MOL (Suppl. Figure 4A).

To induce VIPN, VCR (0.2 mg/kg/week) was administered in adult female rats via the tail vein. MOL (10 or 20 mg/kg/day) was administered daily orally for four weeks, starting on the first day of VCR treatment. Five groups of rats ($n = 12$/group) were randomized as follows: naive untreated (Control); VCR; MOL (20 mg/kg); VCR + MOL (10 mg/kg); and VCR + MOL (20 mg/kg). The animals tolerated the administration of VCR, with a normal weight gain, no behavioral signs of distress, and no mortality reported (Suppl. Figure 4B).

To assess the effect of MOL on axon degeneration, we performed nerve conduction studies (NCS) with a protocol that mirrors a routine examination in any EMG clinical lab[58] at baseline and at the end of treatment. Of note, VCR-treated rats showed a significant decrease in digital sensory action potential (SAP) nerve amplitude and sensory nerve conduction velocity (NCV) that was prevented by MOL administration (Fig. 4A–B). Upon pathologic examination performed on samples obtained at the end of VCR administration, axonopathy was evident in the caudal nerve and was partially prevented by MOL treatment (Fig. 4C–F). Consistent with previous reports[52], no significant changes were observed upon pathological examination of sciatic nerves in VCR-treated rats (data not shown).

To test for the effects of MOL on the development of neuropathic pain-like behavior, we studied withdrawal responses to mechanical stimulation (dynamic plantar mechanical stimulation) at baseline and the end of treatment[59]. The selected schedule of VCR administration induced a robust mechanical hypersensitivity that was prevented by MOL administration (Fig. 4G). We also tested thermal sensitivity (plantar analgesiometer test); however, we did not observe any difference between control and VCR-treated rats (Suppl. Figure 4C). Moreover, at the end of the experiment, VCR-treated animals had a significant decrease in intraepidermal nerve fiber (IENF) density in comparison to control rats. Importantly, IENF density loss was robustly prevented by MOL treatment (Fig. 4H). Altogether, these results reveal the neuroprotective potential of MOL and warrant future investigations of this drug as a therapeutic agent to prevent VIPN.

Discussion

In this study, we conducted a comprehensive screening for small molecules to interrogate the pathways underlying VCR-induced axonopathy as a way to inform targeted therapies for VIPN. Our findings demonstrate that SIN-1, an active metabolite of MOL, effectively prevents VCR-induced axon loss in both motor and sensory neurons without compromising the anticancer efficacy of VCR. We also provide compelling evidence that the neuroprotective effect of SIN-1 is mediated through the activation of sGC, as evidenced by the attenuation of SIN-1 neuroprotection with sGC inhibitors and the mimicking of neuroprotection with sGC activators. Importantly, our study highlights the potential of MOL as a therapeutic strategy to prevent VIPN. Co-administration of MOL with VCR significantly reduced the severity of VIPN in rats, as evidenced by electrophysiological and behavioral assessments. Furthermore, we identified cGMP levels as a potential biomarker of VCR-induced neurotoxicity, suggesting its utility as a companion diagnostic for optimizing MOL and VCR combinatorial regimens in VIPN prevention. Whether cGMP levels could also be used to identify patients with a greater risk of developing VIPN would be worth considering to improve personalized treatment in cancer patients.

A limitation of our screening platform is the use of ES-derived motor neurons as a primary screening assay, which could potentially miss relevant hits. Since we aim to find compounds that work both on motor and sensory neurons, we strengthened our screening platform by combining primary screening in ES-derived motor neurons with secondary screening in motor and sensory neurons from both embryonic and adult mouse stages. This approach sets our study apart from previous screens that primarily relied on neuronal-like cell lines such as PC12 cells, (SH)-SY5Y cells, and immortalized DRG neurons[60]. Our screening methodology's reliability is highlighted by identifying compounds whose targets have been previously implicated in axon degeneration. For instance, we identified SB 239063, a potent and specific p38 MAP kinase inhibitor previously shown to delay axon degeneration in sensory neurons[61]. In addition, we have identified ruthenium red, a non-selective Ca^{2+} channel blocker,
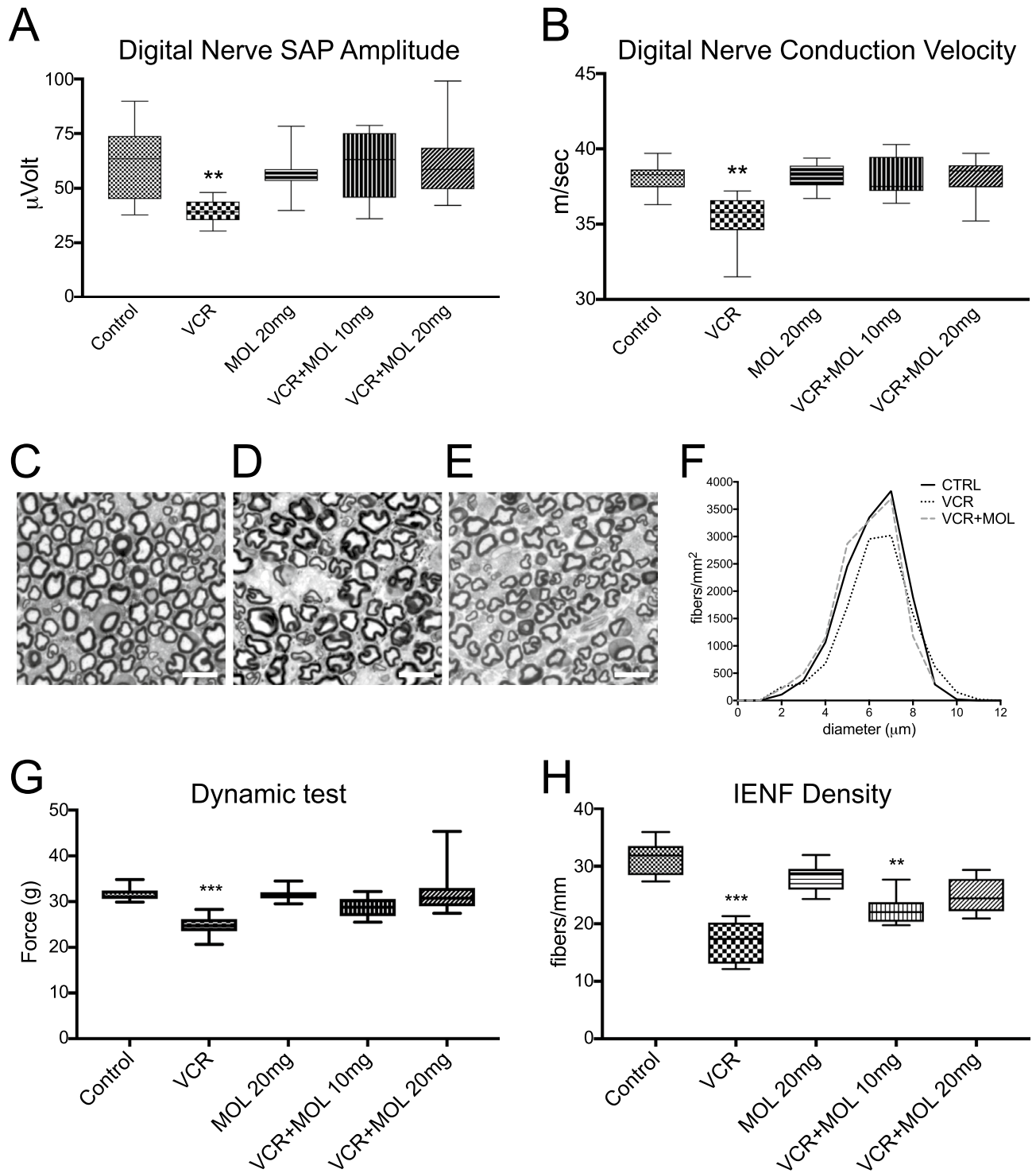
Figure 4. Molsidomine provides neuroprotection in a rat model of vincristine-induced peripheral neurotoxicity. (**A–B**) Neurophysiological results obtained at the end of treatment in digital nerves in Sensory Action Potential (SAP) amplitude and sensory and motor conduction velocity. Treatment with 20 mg/kg of MOL restores Sensory Action Potential (SAP) (A) and nerve Conduction Velocity (NCV) (**B**) of digital nerve altered by VCR to the level of Control. Data are presented as median ± interquartile range ($n = 12$; One-Way ANOVA with Tukey post-hoc test; **$p < 0.01$). (**C–E**) Caudal nerves in control (**C**), VCR-treated (**D**), and VCR + MOL-treated (**E**) rats. Note that VCR alone (**D**) induces shrinkage of myelinated axons and swelling of extracellular space, and molsidomine cotreatment (**E**) partially restores the normal ultrastructure of myelinated fibers. Scale bar, 10 μm. (**F**) Quantification of caudal nerve fiber density in samples from **C–E**. Molsidomine treatment preserves the nerve density in the caudal nerve. Note that the diameter of axons is preserved in the VCR + MOL group to the level in the Control group, and density is presented as fibers per mm². Mean ± SEM. One-Way ANOVA on ranks, (**G**) Treatment with 20 mg/kg of MOL restores a sensitivity threshold to applied mechanical forces decreased by VCR to the level of Control. Data are presented as median ± interquartile range ($n = 12$; One-Way ANOVA with Tukey post-hoc test; ***$p < 0.001$). (**H**) Intraepidermal nerve fiber density (IENF) is preserved in MOL-treated groups compared to VCR. Data are presented as median ± interquartile range (one-way ANOVA and the Tukey–Kramer post-test, $n = 3$; **$p < 0.01$, ***$p < 0.001$). See also Figure S4.

which was reported to inhibit paclitaxel-induced thermal hyperalgesia in rats[62]. Moreover, our platform has the potential for extension to other chemotherapy agents, such as paclitaxel and bortezomib, as well as to different disease states like diabetic peripheral neuropathy, where axonopathy is a prominent neuropathological feature[63].

To ensure our findings' clinical relevance and safety, we incorporated a counter-screen using immortalized lines from cancer patients commonly treated with VCR[64]. This step eliminates protective compounds that might compromise VCR's anti-cancer effects. Early therapeutic intervention or even preventive treatments could be implemented to simultaneously protect peripheral nerves against VCR-induced neurotoxicity without compromising its therapeutic effects against cancer. Our striking observations warrant further testing, especially with MOL and related compounds, given their readily clinical use in additional VCR-sensitive cell lines and patient-derived xenograft models. One limitation of these studies is the fact that the effects of chemotherapy on the peripheral and central nervous system are investigated in immune-competent animals, while preclinical oncology drug testing is primarily based on the use of immunodeficient tumor-bearing mice. At the cellular and molecular levels, responses in immunodeficient mice might not represent the neuroinflammatory neuropathy phenotypes that develop in VCR-treated cancer patients. Therefore, it would be interesting to create novel immunocompetent tumor-bearing rodent models that simultaneously assess VCR's antineoplastic and neurotoxic effects alone or combined with MOL. Another potential limitation in translating our findings to the clinic is the high concentration of SIN-1 required to counteract the VCR neurotoxic effect in neurons. Our PK studies in rats confirm that we do not reach the high concentration of SIN-1 used in vitro. These sub-optimal doses of SIN-1 could partly explain why neuroprotection upon MOL treatment is incomplete. MOL has been extensively used to treat heart conditions in humans to a dose of up to 40 mg daily[55–57]. This strong safety profile warrants future studies to determine whether higher doses of MOL can be more effective in our in vivo model of VIPN.

Cell-based models are excellent tools for screening and identifying pathways that govern specific pathological processes. However, they often do not recapitulate all pathological aspects of conditions such as CIPN, in which different cell types contribute to the disease manifestation. Therefore, preclinical studies must be conducted using reliable in vivo models to establish the disease relevance of a specific pathway. For our in vivo testing of MOL therapeutic potential, we used a rat model of VIPN, in which intravenous injection of VCR reproduces most of the behavioral, pathological, and physiological alterations observed in cancer patients affected by VIPN[52,65]. Treatment with MOL partially attenuates peripheral neurotoxicity in this rodent model of VIPN. This incomplete neuroprotection upon MOL treatment is most likely the result of a sub-optimal concentration of SIN-1 achieved with the doses of MOL used in this study.

Regarding the role of NO in modulating VIPN, our data align with previous studies that highlight the involvement of the NO/cGMP signaling pathway in VCR-induced hyperalgesia[66–68]. Dysregulation of this pathway appears to contribute to the development of hyperalgesia, as shown by decreased levels of NO-oxidized products, neuronal NOS, and cGMP in VCR-treated mice[66]. In addition, L-arginine and SIN-1 administered intracerebroventricularly to mice cause antinociception[67], as well as intraplantar injection of sodium nitroprusside, a substance that nonenzymatically releases NO[68]. However, there is also evidence that activation of NOS and the cGMP pathway increases nocifensive behavior after VCR treatment[69]. This pronociceptive effect can be reversed by administering NOS inhibitors[69]. These conflicting findings suggest a dual impact of NO on pain perception, with high concentrations intensifying pain and low concentrations reducing it[70,71]. The dual effect of NO depends not only on the doses of the NO donors but also on the experimental model used for pain evaluation and the site of activation[72]. Indeed, intradermal administration of drugs capable of activating the NO/cGMP pathway induces nociceptive phenomena, whereas the subcutaneous injection of these drugs results in analgesia, suggesting the existence of different subsets of nociceptive neurons in which NO plays opposing roles[73]. This discrepancy underscores the complexity of NO's role in synaptic transmission and pain modulation, and further studies are needed to fully elucidate its role in the nociceptive system[74–76].

VCR induces oxidative stress and overproduction of reactive oxygen species (ROS), leading to axonal degeneration and slowing of motor nerve conduction velocity[77]. In this context, a recent study reports a mechanism by which VCR causes a local increase in mitochondrial proteins that produce ROS in the axon[78]. Therefore, considering that increased ROS levels can lead to reduced NO bioavailability[79], it is tempting to speculate that SIN-1 exerts its neuroprotective effect by restoring physiological levels of NO-induced second messengers such as cGMP. Future studies will test this hypothesis by genetic manipulation of the NO-cGMP-PGK signaling pathway to investigate the downstream effects of altered cGMP levels.

In conclusion, our study provides compelling evidence for the value of our screening approach in identifying potential therapeutic strategies to prevent VIPN. The neuroprotective effects of SIN-1, mediated through sGC activation, and the potential of MOL as a preventive agent demonstrate the promise of such therapies to reduce VCR-induced neurotoxicity without compromising its anticancer efficacy.

Methods
Animals and drug treatment
All animal procedures followed the National Institutes of Health Guide for Care and Use of Laboratory Animals (National Research Council, 2011). All animal procedures were approved and performed following the institutional animal care and use committee's policies at Columbia University and in compliance with the ARRIVE guidelines. Male and female mice were group-housed in polycarbonate cages with corncob bedding; they were maintained in a humidity-and temperature-controlled vivarium (20–22 °C) on a 12/12 h light/dark schedule. Animals had access ad libitum to food and water except during behavioral testing. *Pirt::Cre* mice in which Cre recombinase is expressed specifically in all primary sensory neurons in DRG under the control of Pirt promoter were obtained from Dr. X. Dong (Johns Hopkins University). Ai14 mice that express tdTomato fluorescence following Cre-mediated recombination were purchased from The Jackson Laboratory (Strain #:007,914). The

two mouse lines were crossed to obtain a new line of *Pirt*::Cre-tdTomato mice used to culture genetically labeled DRG neurons. Hb9::GFP mice expressing green fluorescent protein (GFP) have been purchased from Jackson Laboratory (Strain #:005,029). For cell culture experiments, we used embryos at the 12.5 embryonic stage.

Experiments with rats were performed in conformity with the Institutional Guidelines in compliance with national (D.L. n. 26/2014, *Gazzetta Ufficiale della Repubblica Italiana,* Serie Generale n.61 del 14-3-2014) and international laws (Directive 2010/63/EU of the European Parliament and of the Council, 2010; Guide for the Care and Use of Laboratory Animals, US National Research Council, 8th ed., 2011). All procedures were conducted following protocols approved by the Ethics Committee of the University of Milan Bicocca and approved by the Italian Ministry of Health (no. 732/2018-PR). Female Wistar rats (175–200 g at the beginning of the study) were purchased from Envigo Laboratory (Udine, Italy). The animals were housed under a 12 h light/dark cycle in the animal facility-controlled rooms (maintained at 22 ± 2 °C with a relative humidity of $55 \pm 10\%$) with ad libitum access to food and water. Throughout the study, the rats were monitored daily for evidence of debilitation due to drug treatments, which is indicated by changes in their appearance (i.e., piloerection, kyphosis, mucosal dehydration, rhinorrhea), behavior (decreased grooming, eating, and drinking) and activity (decreased exploring and nesting). Any animal demonstrating evident signs of distress or affected by a body weight decrease > 20% from the beginning of the study was carefully examined by a certified veterinarian for possible withdrawal from the study.

VCR was purchased as a ready-to-use solution (TEVA Italia S.r.l., Milano, Italy) and injected intravenously (i.v.) once a week for four weeks at a dose of 0.2 mg/kg in a volume of 1 ml/kg. MOL (Sigma-Aldrich, Saint Louis, MO, USA) was dissolved in sterile water and administered daily by oral gavage at 10 or 20 mg/kg/day in a 5 ml/kg volume. All dosing solutions were prepared fresh on each administration day.

Embryonic stem cell motor neuron (ES-MN) culture

Mouse embryonic stem (ES) cells expressing a motor neuron-specific reporter (Hb9:GFP) were established as previously described (Wichterle et al., 2002). ES cells were grown under standard pluripotency maintenance conditions on DR4 irradiated mouse embryonic fibroblast feeder cells (GlobalStem) seeded on 0.1% gelatinized (Millipore, #ES 006-B) tissue culture plates. ES cells were maintained in ES Medium: Embryomax DMEM (Chemicon, #SLM-021-A); 20% HyClone FBS (Cytiva, SH30071.03IR25-40); Glutamine (Gibco, #25,030–081); NEAA (Chemicon, #TMS-001-C); Nucleosides (Chemicon, #ES-008-D); β-Mercaptoethanol (Milipore, #ES-007-E), Na-Pyruvate (Chemicon, #TMS-005-C); Pen/Strep (Gibco, #15,140–112), LIF (final 103 unit/ml, Chemicon ESGRO, #ESG1107).

For MN differentiation, at DIV 3, ES cells were trypsinized with 1X trypsin/EDTA (Gibco, #25,300,120) and cultured in αDFNK media: 1:1 DMEM/F12 (Gibco, #12,634) and Neurobasal A (Gibco, #21,103); 10% Knock-out serum (Invitrogen, #10,828–028); Glutamine (Gibco, #25,030–081); 2-Mercaptoethanol (Millipore, #ES-007-E); Pen/Strep (Gibco, #15,140–112). At DIV 4, forming embryonic bodies (EBs) were transferred in low-adherence plates (TC falcon). At DIV 5, 1 μM of all-trans retinoic acid (RA, Sigma, #R2625) and 0.25 μM of smoothened agonist (SAG, Calbiochem, #566,660) were added for an additional four days. Next, differentiated EB-MNs were dissociated and plated at 1,500 cells/well in 96-well or 400 cells/well in 384-well plates pre-coated with 100 μg/ml of L-Polyornithine followed with 3 μg/ml of Laminin diluted in L15 medium with 0.02% NaHCO$_3$. ES-MNs were cultured in ES-MN Medium (Neurobasal, supplemented with $1 \times$ B27, 2% Horse serum, 2 nM L-Glutamine, 0.25% 2-Mercaptoethanol, $1 \times$ Penicillin/Streptomycin, and growth factors GDNF, BDNF, and CNTF at 10 ng/ml each) for five days (DIV5) before compounds have been applied. ES-MN cultures were imaged daily using an automated reader system (TROPHOS). MN number and neurite length were assessed with the MetaMorph software (Molecular Imaging).

Primary spinal cord motor neuron culture

As previously described, primary motor neurons (pMNs) were prepared from E12.5 embryos of Hb9:GFP transgenic mice[80]. Briefly, spinal cords from 5–6 embryos were collected in an Eppendorf tube with 1 ml cold 0.45% Glucose in PBS, digested with 0.025% trypsin for 5 min, and triturated in 2 ml of L-15 medium supplemented with 0.4% BSA and 200 U/ml DNAse I until complete dissociation to single cells. The final cell suspension was purified via 4% BSA centrifugation at 160 g for 5 min. Cells were cultured in L-Polyornithine (100 μg/ml) and Laminin (3 μg/ml) coated plates at the density of 1,500 GFP + cells/well in the Neurobasal medium supplemented with 2% horse serum (heat inactivated), $1 \times$ B27, 0.5 mM glutamine, 25 μM 2-mercaptoethanol, 1% penicillin/streptomycin and the cocktail of trophic factors: GDNF, BDNF, and CNTF at the concentration of 0.5, 1, and 10 ng/ml, respectively.

Primary DRG sensory neuron culture

Sensory neurons from DRG were prepared from heterozygous *Pirt*::Cre-Ai14 mice expressing tdTomato after Cre recombination under the DRG neuron-specific Pirt promoter. DRG were collected from 12-week-old mice deeply anesthetized with isoflurane. DRG were harvested from cervical, thoracic, and lumbar levels to ensure the presence of neurons from each region of each mouse. Dissociation of DRG began with enzymatic dissociation in 1 ml of MEM medium supplemented with 2.5 mg/ml collagenase A (activity 0.255 U/mg) for 40 min at 37^0 C, followed by incubation in TrypLE for 10 min. Trypsinization was stopped with 10% horse serum, and DRGs were transferred for mechanical trituration in MEM medium supplemented with 100 U/ml DNAse I. Final cell purification was done by centrifugation via 4% BSA (5 min at 1,000 rpm). Approximately 70,000 td-Tomato-positive cells are routinely obtained from 50 DRGs with less than 10% dead cells as determined by Trypan Blue staining. Cells were cultured in 96-well (300 cell/well) or 384-well (125 cells/well) plates coated with L-Polyornithine (100 μg/ml) and Laminin (10 μg/ml) in MEM medium supplemented with $1 \times$ B27, $1 \times$ MEM

vitamins, and $1 \times$ penicillin/streptomycin. Cultured cells were growing in vitro for five days before applying chemical compounds.

Luminescent cell viability assay celltiter-Glo®

Cell viability has been determined by quantitating the ATP levels using CellTiter-Glo®, according to the manufacturer's instructions. CUTLL1 Human T-cell Lymphoblastic Lymphoma (Millipore-Sigma, Cat # SCC286) and OCI-LY1 germinal center diffuse large B cell lymphoma (German Collection of Microorganisms and Cell Cultures GmbH, DSMZ # ACC 722) cell lines have been plated in 384-well plates at 1,000 cells/well in 50 μl of RPMI medium supplemented with 10% FBS, 2 nM L-Glutamine and $1 \times$ Penicillin/Streptomycin. After 18 h of culture, VCR concentrations for the dose–response curve were determined in the range of 0.00001–0.1 μM, and 0.1% DMSO and biomolecules at EC-50 concentration were applied for 24 and 48 h. Twenti-five μl of CellTiter-Glo® Reagent was added to each well for 10 min to develop a luminescent signal detected with the Tecan Infinity 2000 plate reader. The luminescent signal was normalized to DMSO control and expressed in percentage.

Tocris plus library of biomolecules for HTS

The collection of 1,280 biomolecules from the Tocris Plus Library, including biologically active FDA-approved and natural compounds, was used. High-throughput primary screening was performed in the Columbia Genome Center's High Throughput Screening facility equipped with the Perkin Elmer Cell::Explorer robotic platform. For primary screening, each biomolecule was applied to ES-MN cultures at 10 μM in the presence of 2 nM of Vincristine in triplicates. Fluorescent images were acquired using INCell Analyzer 2000 GE, and the FITC filter was used to capture motor neurons expressing GFP. The 4X lens was used to acquire whole-well images of 384-well plates. Exposure time was 1.2 s, and automatic laser focus was used to ensure well-focused images. Analysis was performed with bioinformatics software Pipeline Pilot (Biovia), using a standard deviation (SD) multiplier equal to 2.0.

Measurement of intracellular cGMP levels

Intracellular cGMP levels were measured using an ELISA kit according to the manufacturer's instructions (ADI-900-014, Enzo Life Sciences, USA). Briefly, 1×10^6 ES-MNs were treated for 4 h with DMSO (0.1%), VCR (2 nM), SIN-1 (50 μM), and ODQ (10 μM) alone or in combination (VCR + SIN-1 or SIN-1 + ODQ). After treatment, ES-MNs were washed once with PBS and lysed with 1 mL of 0.1 M HCl + 0.1% Triton-X at room temperature for 10 min with intermittent vortexing. Samples were centrifuged for 10 min at 10,000 to remove cellular debris. The protein concentration was determined using the Bradford method, and equal amounts of total protein (10 μg) were used to measure cGMP levels using the non-acetylated protocol. All samples and standards were assayed in duplicate. Absorbance was measured at 405 nm using an EnVision plate reader (PerkinElmer, Waltham, Massachusetts). The detection ranges for cGMP were 0.8 to 500 pmol/ml. cGMP values were presented as pmol/mg protein.

Nerve conduction studies

Neurophysiological recordings were performed in the caudal and digital nerves at baseline and end of treatment to determine peripheral sensory/motor nerve functional status, as previously reported[58]. Electrophysiological recordings were performed with an electromyography apparatus (Myto2 ABN Neuro, Firenze, Italy). All recordings were performed with a subdermal EEG needle (Ambu Neuroline; Ambu, Ballerup, Denmark).

The caudal nerve was recorded by placing a couple of recording needle electrodes at the base of the tail and a couple of stimulating needle electrodes 3 cm distally to the recording points. Similarly, the digital nerve was recorded by placing the recording electrodes close to the ankle bone and the stimulating electrodes close to the fourth toe near the digital nerve. The caudal and digital sensory NCV were calculated by measuring the latency between the stimulus artifact and the onset of the first peak of the elicited response and the distance between the recording and the stimulating points. SAP amplitude was also measured. Intensity, duration, and stimulation frequency were set up to obtain supramaximal results. Animals were kept under deep isoflurane anesthesia, and body temperature was kept constant at 34.5 ± 0.5 °C.

Dynamic plantar aesthesiometer test

The Dynamic Plantar Aesthesiometer (model 37,450; Ugo Basile Biological Instruments, Comerio, Italy) was used to evaluate the mechanical allodynia on the plantar surface to mechanical stimuli. Rats were placed individually in a Plexiglas chamber and allowed to acclimatize to the testing environment for at least 15 min. The hind paw withdrawal threshold was recorded automatically and determined by calculating the mean value of six repeated applications to the plantar surface. A metal filament exerted a progressively increasing puncture pressure, reaching up to 50 g within 20 s, and was applied to the central region on the plantar surface. A cut-off time of 30 s was used to prevent tissue damage.

Plantar analgesiometer test

Two hours after the dynamic test evaluation, the response to the noxious thermal stimulus was determined using a Plantar Analgesiometer (model 37,370; Ugo Basile Biological Instruments, Comerio, Italy). The rats were placed into a Plexiglas chamber for a 15-min acclimatization period followed by testing. A movable infrared radiant heat source (IR 40) was placed directly under the plantar surface on the hind paw. The nociceptive threshold response to the thermal stimulus was determined by calculating the mean value of four repeated measures. A

cut-off time of 30 s was used to avoid any tissue damage. Both behavioral tests were performed at baseline and the end of treatment.

Morphological and morphometric examination of caudal nerves

Samples for morphological and morphometric studies were obtained after deep anesthesia at the sacrifice stage. The caudal nerve was obtained from 4 animals to each group fixed in 3% glutaraldehyde in phosphate buffer solution 0.12 M, pH 7.4, followed by OsO_4 post-fixation and embedded in epoxy resin. Semithin sections of 1.5 μm thickness were stained with toluidine blue and used for morphological observation, performed with a Nikon Eclipse E200 light microscope (Nikon, Firenze, Italy).

For morphometric examination, the caudal nerves of three animals per group were analyzed; for each animal, three randomly selected fields/animals were taken at 60X with a Nikon Eclipse E200 light microscope (Nikon, Firenze, Italy). The pictures were analyzed using an automatic image analyzer (Immagini Computer SNC, Milan, Italy), and the data were processed with GraphPad Prism version 7 (GraphPad Software, San Diego, CA).

Intra epidermal nerve *fiber* density

Skin biopsies from four animals from each group were collected and immediately fixed by immersion in PLP 2% (paraformaldehyde-lysine-sodium periodate fixative solution) for 24 h at 4 °C. Then, the samples were cryoprotected (20% glycerol, 20% PBS, 60% dH_2O solution) at -20 °C and serially cut with a cryostat to obtain 20-μm sections. Three sections from each sample were randomly selected and immunostained with protein gene product 9.5 antibodies (PGP 9.5; GeneTex, Irvine CA, USA, cat#GTX109637; 1:100 dilution) using a free-floating protocol[81]. Briefly, sections were blocked with 0.1% triton X-100 and 4% normal goat serum in TBS solution for one hour and then incubated overnight with anti-PGP 9.5 antibodies. After rinsing, sections were incubated with biotinylated goat anti-rabbit IgG for 1 h (1:100 dilution, Vector, Burlingame CA, USA, cat# BA-1000). Then, the sections were placed in 33% methanol/PBS with 3.3% H_2O_2 for 30 min, then in avidin–biotin complex (Vector, Burlingame CA, USA) for one h. The reaction product was demonstrated by the blue chromogen/peroxidase substrate (SG substrate kit, Vector, Burlingame, CA, USA). The number of positive IENFs was counted under a light microscope at high magnification (40X). The length of the epidermis was measured, and the density of IENF was obtained as a ratio between the number of positive IENF and the epidermis size.

Statistical analysis

Continuous variables were reported as percentages or means ± standard error of the mean (SEM), as appropriate. Differences in body weight, NCV, sensory potential amplitude, behavioral tests, and IENF density were statistically evaluated using the non-parametric Kruskal–Wallis test, followed by the pair-wise Dunns post-hoc test. The differences among means were analyzed by a parametric one-way ANOVA followed by pair-wise Tukey's posthoc test for all other variables. All analyses rejected the null hypothesis at the 0.05 level and reported as follows: $* = p < 0.05$; $** = p < 0.01$; $*** = p < 0.001$; $**** = p < 0.0001$. All analyses were performed with GraphPad Prism version 7 (GraphPad Inc. La Jolla CA, USA).

Data availability

The datasets used and/or analysed during the current study are available from the corresponding author upon reasonable request.

References

1. Alberti, P. *et al.* Neurological complications of conventional and novel anticancer treatments. *Cancers* https://doi.org/10.3390/cancers14246088 (2022).
2. Boyette-Davis, J. A., Walters, E. T. & Dougherty, P. M. Mechanisms involved in the development of chemotherapy-induced neuropathy. *Pain Manag.* **5**, 285–296. https://doi.org/10.2217/pmt.15.19 (2015).
3. Cavaletti, G. & Marmiroli, P. Chemotherapy-induced peripheral neurotoxicity. *Curr Opin Neurol* **28**, 500–507. https://doi.org/10.1097/WCO.0000000000000234 (2015).
4. Corbin, Z. A. *et al.* Characterization of the peripheral neuropathy associated with brentuximab vedotin treatment of mycosis fungoides and sezary syndrome. *J. Neurooncol.* **132**, 439–446. https://doi.org/10.1007/s11060-017-2389-9 (2017).
5. Vahdat, L. T. *et al.* Ixabepilone-associated peripheral neuropathy: Data from across the phase II and III clinical trials. *Supp. Care Cancer* **20**, 2661–2668. https://doi.org/10.1007/s00520-012-1384-0 (2012).
6. Hershman, D. L. *et al.* Comorbidities and risk of chemotherapy-induced peripheral neuropathy among participants 65 years or older in southwest oncology group clinical trials. *J. Clin. Oncol.* **34**, 3014–3022. https://doi.org/10.1200/JCO.2015.66.2346 (2016).
7. Cavaletti, G. *et al.* Patients' and physicians' interpretation of chemotherapy-induced peripheral neurotoxicity. *J. Peripher. Nerv. Syst.* **24**, 111–119. https://doi.org/10.1111/jns.12306 (2019).
8. Seretny, M. *et al.* Incidence, prevalence, and predictors of chemotherapy-induced peripheral neuropathy: A systematic review and meta-analysis. *Pain* **155**, 2461–2470. https://doi.org/10.1016/j.pain.2014.09.020 (2014).
9. Pachman, D. R. *et al.* Clinical course of oxaliplatin-induced neuropathy: Results from the randomized phase III trial N08CB (alliance). *J. Clin. Oncol.* **33**, 3416–3422. https://doi.org/10.1200/JCO.2014.58.8533 (2015).
10. Park, S. B. *et al.* Chemotherapy-induced peripheral neurotoxicity: A critical analysis. *CA Cancer J. Clin.* **63**, 419–437. https://doi.org/10.3322/caac.21204 (2013).
11. Loprinzi, C. L. *et al.* Prevention and management of chemotherapy-induced peripheral neuropathy in survivors of adult cancers: ASCO guideline update. *J. Clin. Oncol.* **38**, 3325–3348. https://doi.org/10.1200/JCO.20.01399 (2020).
12. Dorsey, S. G. *et al.* NCI clinical trials planning meeting for prevention and treatment of chemotherapy-induced peripheral neuropathy. *J. Natl. Cancer Inst.* https://doi.org/10.1093/jnci/djz011 (2019).
13. Mora, E., Smith, E. M., Donohoe, C. & Hertz, D. L. Vincristine-induced peripheral neuropathy in pediatric cancer patients. *Am. J. Cancer Res.* **6**, 2416–2430 (2016).

14. Gilchrist, L. & Tanner, L. Gait patterns in children with cancer and vincristine neuropathy. *Pediatr. Phys. Ther.* **28**, 16–22. https://doi.org/10.1097/PEP.0000000000000208 (2016).
15. Islam, B. *et al.* Vinca alkaloids, thalidomide and eribulin-induced peripheral neurotoxicity: From pathogenesis to treatment. *J. Peripher. Nerv. Syst.* **24**(Suppl 2), S63–S73. https://doi.org/10.1111/jns.12334 (2019).
16. Schloss, J. M. *et al.* A randomised, placebo-controlled trial assessing the efficacy of an oral B group vitamin in preventing the development of chemotherapy-induced peripheral neuropathy (CIPN). *Supp. Care Cancer* **25**, 195–204. https://doi.org/10.1007/s00520-016-3404-y (2017).
17. Kautio, A. L. *et al.* Amitriptyline in the prevention of chemotherapy-induced neuropathic symptoms. *Anticancer Res.* **29**, 2601–2606 (2009).
18. Bradfield, S. M., Sandler, E., Geller, T., Tamura, R. N. & Krischer, J. P. Glutamic acid not beneficial for the prevention of vincristine neurotoxicity in children with cancer. *Pediatr. Blood Cancer* **62**, 1004–1010. https://doi.org/10.1002/pbc.25384 (2015).
19. Majithia, N. *et al.* National cancer institute-supported chemotherapy-induced peripheral neuropathy trials: Outcomes and lessons. *Support Care Cancer* **24**, 1439–1447. https://doi.org/10.1007/s00520-015-3063-4 (2016).
20. Berbusse, G. W., Woods, L. C., Vohra, B. P. & Naylor, K. Mitochondrial dynamics decrease prior to axon degeneration induced by vincristine and are partially rescued by overexpressed cytNmnat1. *Front. Cell. Neurosci.* **10**, 179. https://doi.org/10.3389/fncel.2016.00179 (2016).
21. Geisler, S. *et al.* Prevention of vincristine-induced peripheral neuropathy by genetic deletion of SARM1 in mice. *Brain J. Neurol.* **139**, 3092–3108. https://doi.org/10.1093/brain/aww251 (2016).
22. Ji, X. T. *et al.* Spinal astrocytic activation contributes to mechanical allodynia in a rat chemotherapy-induced neuropathic pain model. *PLoS One* **8**, e60733. https://doi.org/10.1371/journal.pone.0060733 (2013).
23. Montague, K., Simeoli, R., Valente, J. & Malcangio, M. A novel interaction between CX3CR1 and CCR2 signalling in monocytes constitutes an underlying mechanism for persistent vincristine-induced pain. *J. Neuroinflamm.* **15**, 101. https://doi.org/10.1186/s12974-018-1116-6 (2018).
24. Old, E. A. *et al.* Monocytes expressing CX3CR1 orchestrate the development of vincristine-induced pain. *J. Clin. Invest.* **124**, 2023–2036. https://doi.org/10.1172/JCI71389 (2014).
25. Shen, Y. *et al.* Exogenous induction of HO-1 alleviates vincristine-induced neuropathic pain by reducing spinal glial activation in mice. *Neurobiol. Dis.* **79**, 100–110. https://doi.org/10.1016/j.nbd.2015.04.012 (2015).
26. Van Helleputte, L. *et al.* Inhibition of histone deacetylase 6 (HDAC6) protects against vincristine-induced peripheral neuropathies and inhibits tumor growth. *Neurobiol. Dis.* **111**, 59–69. https://doi.org/10.1016/j.nbd.2017.11.011 (2018).
27. Zhou, L. *et al.* Levo-corydalmine alleviates vincristine-induced neuropathic pain in mice by inhibiting an NF-kappa B-dependent CXCL1/CXCR2 signaling pathway. *Neuropharmacology* **135**, 34–47. https://doi.org/10.1016/j.neuropharm.2018.03.004 (2018).
28. Neukomm, L. J. & Freeman, M. R. Diverse cellular and molecular modes of axon degeneration. *Trends Cell. Biol.* **24**, 515–523. https://doi.org/10.1016/j.tcb.2014.04.003 (2014).
29. Conforti, L., Gilley, J. & Coleman, M. P. Wallerian degeneration: an emerging axon death pathway linking injury and disease. *Nat. Rev. Neurosci.* **15**, 394–409. https://doi.org/10.1038/nrn3680 (2014).
30. Geisler, S. *et al.* Vincristine and bortezomib use distinct upstream mechanisms to activate a common SARM1-dependent axon degeneration program. *JCI Insight* https://doi.org/10.1172/jci.insight.129920 (2019).
31. Liu, H. W. *et al.* Pharmacological bypass of NAD(+) salvage pathway protects neurons from chemotherapy-induced degeneration. *Proc. Natl. Acad. Sci. USA* **115**, 10654–10659. https://doi.org/10.1073/pnas.1809392115 (2018).
32. Turkiew, E., Falconer, D., Reed, N. & Hoke, A. Deletion of Sarm1 gene is neuroprotective in two models of peripheral neuropathy. *J. Peripher. Nerv. Syst.* **22**, 162–171. https://doi.org/10.1111/jns.12219 (2017).
33. Li, H. *et al.* Protein prenylation constitutes an endogenous brake on axonal growth. *Cell Rep.* **16**, 545–558. https://doi.org/10.1016/j.celrep.2016.06.013 (2016).
34. Simon, C. M. *et al.* A stem cell model of the motor circuit uncouples motor neuron death from hyperexcitability induced by SMN deficiency. *Cell Rep.* **16**, 1416–1430. https://doi.org/10.1016/j.celrep.2016.06.087 (2016).
35. Wichterle, H., Lieberam, I., Porter, J. A. & Jessell, T. M. Directed differentiation of embryonic stem cells into motor neurons. *Cell* **110**, 385–397 (2002).
36. Hattori, H. *et al.* Small-molecule screen identifies reactive oxygen species as key regulators of neutrophil chemotaxis. *Proc. Natl. Acad. Sci. USA* **107**, 3546–3551. https://doi.org/10.1073/pnas.0914351107 (2010).
37. Li, X. *et al.* Small-molecule-driven direct reprogramming of mouse fibroblasts into functional neurons. *Cell Stem Cell* **17**, 195–203. https://doi.org/10.1016/j.stem.2015.06.003 (2015).
38. Yu, C. *et al.* Small molecules enhance CRISPR genome editing in pluripotent stem cells. *Cell Stem Cell* **16**, 142–147. https://doi.org/10.1016/j.stem.2015.01.003 (2015).
39. Posimo, J. M. *et al.* Viability assays for cells in culture. *J. Vis. Exp.* https://doi.org/10.3791/50645 (2014).
40. Zhang, J. H., Chung, T. D. & Oldenburg, K. R. A simple statistical parameter for use in evaluation and validation of high throughput screening assays. *J. Biomol. Screen* **4**, 67–73. https://doi.org/10.1177/108705719900400206 (1999).
41. Sui, Y. & Wu, Z. Alternative statistical parameter for high-throughput screening assay quality assessment. *J. Biomol. Screen* **12**, 229–234. https://doi.org/10.1177/1087057106296498 (2007).
42. Ikiz, B. *et al.* The regulatory machinery of neurodegeneration in in vitro models of amyotrophic lateral sclerosis. *Cell Rep.* **12**, 335–345. https://doi.org/10.1016/j.celrep.2015.06.019 (2015).
43. Re, D. B. *et al.* Necroptosis drives motor neuron death in models of both sporadic and familial ALS. *Neuron* **81**, 1001–1008. https://doi.org/10.1016/j.neuron.2014.01.011 (2014).
44. Cirrincione, A. M. *et al.* Paclitaxel-induced peripheral neuropathy is caused by epidermal ROS and mitochondrial damage through conserved MMP-13 activation. *Sci. Rep.* **10**, 3970. https://doi.org/10.1038/s41598-020-60990-8 (2020).
45. Tang, Z. *et al.* Pirt functions as an endogenous regulator of TRPM8. *Nat. Commun.* **4**, 2179. https://doi.org/10.1038/ncomms3179 (2013).
46. Kalac, M. *et al.* HDAC inhibitors and decitabine are highly synergistic and associated with unique gene-expression and epigenetic profiles in models of DLBCL. *Blood* **118**, 5506–5516. https://doi.org/10.1182/blood-2011-02-336891 (2011).
47. Palomero, T. *et al.* CUTLL1, a novel human T-cell lymphoma cell line with t(7;9) rearrangement, aberrant NOTCH1 activation and high sensitivity to gamma-secretase inhibitors. *Leukemia* **20**, 1279–1287. https://doi.org/10.1038/sj.leu.2404258 (2006).
48. Ignarro, L. J., Napoli, C. & Loscalzo, J. Nitric oxide donors and cardiovascular agents modulating the bioactivity of nitric oxide: An overview. *Circ. Res* **90**, 21–28. https://doi.org/10.1161/hh0102.102330 (2002).
49. Feelisch, M., Ostrowski, J. & Noack, E. On the mechanism of NO release from sydnonimines. *J. Cardiovasc. Pharmacol.* **14**(Suppl 11), S13-22 (1989).
50. Fraccarollo, D. *et al.* Soluble guanylyl cyclase activation improves progressive cardiac remodeling and failure after myocardial infarction. Cardioprotection over ACE inhibition. *Basic Res. Cardiol.* **109**, 421. https://doi.org/10.1007/s00395-014-0421-1 (2014).
51. Sawa, T. *et al.* Formation, signaling functions, and metabolisms of nitrated cyclic nucleotide. *Nitric Oxide* **34**, 10–18. https://doi.org/10.1016/j.niox.2013.04.004 (2013).
52. Meregalli, C. *et al.* Neurofilament light chain as disease biomarker in a rodent model of chemotherapy induced peripheral neuropathy. *Exp. Neurol.* **307**, 129–132. https://doi.org/10.1016/j.expneurol.2018.06.005 (2018).

53. Minaz, N. & Razdan, R. Therapeutic insight into molsidomine, a nitric oxide donor in streptozotocin-induced diabetic nephropathy in rats. *Indian J. Pharmacol.* **48**, 544–549. https://doi.org/10.4103/0253-7613.190744 (2016).

54. Fromson, J. M. *et al.* Absorption and disposition of [14C]-molsidomine in laboratory animals. *Arzneimittelforschung* **31**, 337–345 (1981).

55. Meinertz, T. *et al.* Relationship between pharmacokinetics and pharmacodynamics of molsidomine and its metabolites in humans. *Am. Heart J.* **109**, 644–648 (1985).

56. Ostrowski, J. & Resag, K. Pharmacokinetics of molsidomine in humans. *Am. Heart J.* **109**, 641–643 (1985).

57. Rosenkranz, B., Winkelmann, B. R. & Parnham, M. J. Clinical pharmacokinetics of molsidomine. *Clin. Pharmacokinet.* **30**, 372–384. https://doi.org/10.2165/00003088-199630050-00004 (1996).

58. Monza, L., Fumagalli, G., Chiorazzi, A. & Alberti, P. Translating morphology from bench side to bed side via neurophysiology: 8-min protocol for peripheral neuropathy research. *J. Neurosci. Methods* **363**, 109323. https://doi.org/10.1016/j.jneumeth.2021.109323 (2021).

59. Meregalli, C. *et al.* Human intravenous immunoglobulin alleviates neuropathic symptoms in a rat model of paclitaxel-induced peripheral neurotoxicity. *Int. J. Mol. Sci.* https://doi.org/10.3390/ijms22031058 (2021).

60. Lehmann, H. C., Staff, N. P. & Hoke, A. Modeling chemotherapy induced peripheral neuropathy (CIPN) in vitro: Prospects and limitations. *Exp. Neurol.* **326**, 113140. https://doi.org/10.1016/j.expneurol.2019.113140 (2020).

61. Rudhard, Y. *et al.* Identification of 12/15-lipoxygenase as a regulator of axon degeneration through high-content screening. *J. Neurosci.* **35**, 2927–2941. https://doi.org/10.1523/JNEUROSCI.2936-14.2015 (2015).

62. Hara, T. *et al.* Effect of paclitaxel on transient receptor potential vanilloid 1 in rat dorsal root ganglion. *Pain* **154**, 882–889. https://doi.org/10.1016/j.pain.2013.02.023 (2013).

63. Feldman, E. L., Nave, K. A., Jensen, T. S. & Bennett, D. L. H. New horizons in diabetic neuropathy: Mechanisms, bioenergetics, and pain. *Neuron* **93**, 1296–1313. https://doi.org/10.1016/j.neuron.2017.02.005 (2017).

64. Skubnik, J., Pavlickova, V. S., Ruml, T. & Rimpelova, S. Vincristine in combination therapy of cancer: Emerging trends in clinics. *Biology* https://doi.org/10.3390/biology10090849 (2021).

65. Weng, H. R., Cordella, J. V. & Dougherty, P. M. Changes in sensory processing in the spinal dorsal horn accompany vincristine-induced hyperalgesia and allodynia. *Pain* **103**, 131–138 (2003).

66. Kamei, J., Tamura, N. & Saitoh, A. Possible involvement of the spinal nitric oxide/cGMP pathway in vincristine-induced painful neuropathy in mice. *Pain* **117**, 112–120. https://doi.org/10.1016/j.pain.2005.05.026 (2005).

67. Chung, E. *et al.* Dynorphin-mediated antinociceptive effects of L-arginine and SIN-1 (an NO donor) in mice. *Brain Res. Bull.* **70**, 245–250. https://doi.org/10.1016/j.brainresbull.2006.05.008 (2006).

68. Durate, I. D., Lorenzetti, B. B. & Ferreira, S. H. Peripheral analgesia and activation of the nitric oxide-cyclic GMP pathway. *Eur. J. Pharmacol.* **186**, 289–293. https://doi.org/10.1016/0014-2999(90)90446-d (1990).

69. Bujalska, M. & Gumulka, S. W. Effect of cyclooxygenase and nitric oxide synthase inhibitors on vincristine induced hyperalgesia in rats. *Pharmacol. Rep.* **60**, 735–741 (2008).

70. Prado, W. A., Schiavon, V. F. & Cunha, F. Q. Dual effect of local application of nitric oxide donors in a model of incision pain in rats. *Eur. J. Pharmacol.* **441**, 57–65 (2002).

71. Sousa, A. M. & Prado, W. A. The dual effect of a nitric oxide donor in nociception. *Brain Res.* **897**, 9–19. https://doi.org/10.1016/s0006-8993(01)01995-3 (2001).

72. Cury, Y., Picolo, G., Gutierrez, V. P. & Ferreira, S. H. Pain and analgesia: The dual effect of nitric oxide in the nociceptive system. *Nitric. Oxide* **25**, 243–254. https://doi.org/10.1016/j.niox.2011.06.004 (2011).

73. Vivancos, G. G., Parada, C. A. & Ferreira, S. H. Opposite nociceptive effects of the arginine/NO/cGMP pathway stimulation in dermal and subcutaneous tissues. *Br. J. Pharmacol.* **138**, 1351–1357. https://doi.org/10.1038/sj.bjp.0705181 (2003).

74. Bavencoffe, A., Chen, S. R. & Pan, H. L. Regulation of nociceptive transduction and transmission by nitric oxide. *Vitam. Horm.* **96**, 1–18. https://doi.org/10.1016/B978-0-12-800254-4.00001-5 (2014).

75. Park, A. R., Lee, H. I., Semjid, D., Kim, D. K. & Chun, S. W. Dual effect of exogenous nitric oxide on neuronal excitability in rat substantia gelatinosa neurons. *Neural Plast.* **2014**, 628531. https://doi.org/10.1155/2014/628531 (2014).

76. Li, D. Y. *et al.* Targeting the nitric oxide/cGMP signaling pathway to treat chronic pain. *Neural Regen. Res.* **18**, 996–1003. https://doi.org/10.4103/1673-5374.355748 (2023).

77. Jaggi, A. S. & Singh, N. Mechanisms in cancer-chemotherapeutic drugs-induced peripheral neuropathy. *Toxicology* **291**, 1–9. https://doi.org/10.1016/j.tox.2011.10.019 (2012).

78. Gomez-Deza, J., Slavutsky, A. L., Nebiyou, M. & Le Pichon, C. E. Local production of reactive oxygen species drives vincristine-induced axon degeneration. *Cell Death Dis.* **14**, 807. https://doi.org/10.1038/s41419-023-06227-8 (2023).

79. Matsubara, K., Higaki, T., Matsubara, Y. & Nawa, A. Nitric oxide and reactive oxygen species in the pathogenesis of preeclampsia. *Int. J. Mol. Sci.* **16**, 4600–4614. https://doi.org/10.3390/ijms16034600 (2015).

80. Nagai, M. *et al.* Astrocytes expressing ALS-linked mutated SOD1 release factors selectively toxic to motor neurons. *Nat. Neurosci.* **10**, 615–622. https://doi.org/10.1038/nn1876 (2007).

81. Pozzi, E. *et al.* Paclitaxel, but not cisplatin, affects satellite glial cells in dorsal root ganglia of rats with chemotherapy-induced peripheral neurotoxicity. *Toxics* https://doi.org/10.3390/toxics11020093 (2023).

Acknowledgements

Author contributions

F.L. designed and supervised the study. I.U-S. and A.C. designed and performed experiments analysed data and contributed equally to this work. M. dP-S., H.L., C.M, E.P., V.C., A.C., L.M., P.A., and G.F. performed experiments. C.K., Y.M., S.P., and G.C. contributed to data design, analysis, revision, and interpretation. I.U-S., A.C., G.C., and F.L. wrote the paper with input from all the authors.

Competing interests

F. L. is a co-founder and President of a startup company working on antisense oligonucleotide therapeutics. The rest of the authors do not have any competing interests.

Additional information

Supplementary Information The online version contains supplementary material available at https://doi.org/10.1038/s41598-024-70294-w.

Correspondence and requests for materials should be addressed to F.L.

Reprints and permissions information is available at www.nature.com/reprints.

Publisher's note Springer Nature remains neutral with regard to jurisdictional claims in published maps and institutional affiliations.